

1
2 **Spurious Arrivals in Teleseismic Noise Correlations Explained by a Quasi-Stationary**
3 **Phase Condition**
4

5
6 **Lei Li, Pierre Boué, and Michel Campillo**

7
8 Université Grenoble Alpes, CNRS, IRD, IFSTTAR, ISTERre, 38000 Grenoble, France.
9

10
11 **Corresponding author:** Lei Li (lei.li@univ-grenoble-alpes.fr)
12

13 **Key Points:**

- 14 • A prominent P-type phase having no correspondence with the Green's functions of Earth
15 is observed in teleseismic noise correlations.
- 16 • Double-array analysis reveals that the spurious phase originates from the interference
17 between P and PKPab waves with distinct slownesses.
- 18 • Synthetic simulations reproduce the observed spurious phase.
19
20

21 **Abstract**

22 Traditionally, the reconstruction of seismic phases from inter-receiver noise correlations is
23 attributed to the interference between waves from noise sources in the stationary-phase regions.
24 With seismic noise records from two networks at teleseismic distance, we show that spurious
25 signals having no correspondence in real seismograms can arise from interference between
26 waves without common ray path or common slowness. These noise-derived signals cannot be
27 explained by traditional stationary-phase arguments. These signals still emerge for evenly
28 distributed noise sources, and thus are not caused by localized sources. With numerical
29 experiments, we interpret the presence of the spurious signals with a condition of quasi-
30 stationary phase: when time delays between interfering waves from spatially distributed noise
31 sources are close enough, the stack of correlation functions over the distributed sources can be
32 constructive, and thereby noise-derived signals emerge from the source averaging.

33

34 **Plain Language Summary**

35 Noise-based seismic imaging is an emerging technique in deep-Earth seismology. The key of the
36 technique is the extraction of signals from ambient wavefields by correlation of continuous
37 seismic records (a.k.a. ambient noise). A difficulty is that in addition to the expected physical
38 arrivals, some spurious phases without correspondence in earthquake seismograms are observed.
39 It is important to understand precisely their origins, and to evaluate their potential for imaging.
40 Here we study correlations between noise records from two distant networks, one in Finland and
41 the other in Japan. We observe a strong spurious phase from the noise correlations. To
42 understand its origin, we measure travel times and slownesses of the correlated waves and
43 compare with predictions from a reference model. This allows unambiguous identification of the
44 waves that interfere to produce the spurious phase. The identification is further confirmed by the
45 global excitation of seismic noise deduced from oceanographic data. Unexpectedly, the
46 appearance of the spurious phase does not correspond with the condition of stationary phase, as
47 is the case for the actual physical phases. We introduce a less restrictive condition of quasi-
48 stationary phase that is well adapted to finite-frequency seismic wavefields, to interpret the
49 presence of the spurious phase.

50

51 **1 Introduction**

52 The technique of noise correlation is implemented simply via computation of the
53 correlation functions between ambient noise records at receivers. Theoretical and experimental
54 studies (e.g., Lobkis & Weaver, 2001; Wapenaar, 2004) have shown that under restrictive
55 conditions, the inter-receiver correlation function converges toward the response that would be
56 recorded at one receiver if a source was located at the other. This is, by definition, the Green's
57 function of the medium between the two receivers. Great achievements have been realized with
58 the introduction of the noise correlation technique into solid-Earth seismology (Campillo & Paul,
59 2003; Shapiro & Campillo, 2004). The most common applications are passive imaging (e.g.,
60 Sabra et al., 2005; Shapiro et al., 2005) and monitoring (e.g., Brenguier et al., 2008; Wegler et
61 al., 2009) of the subsurface using signals derived from seismic noise. We refer to (Campillo &
62 Roux, 2015) for a systematic review on the recent progress in the theoretical and methodological
63 aspects, and the various noise-based applications.

64 Both the surface-wave and body-wave parts of the Green's function can be reconstructed
 65 from noise correlations. Surface waves are easier to extract due to their dominance in the noise
 66 power spectra. There are relatively few, yet promising, examples of noise-derived body waves.
 67 Recently, it has been demonstrated that deep body-wave signals that propagate through the
 68 mantle and core can be extracted from ambient noise correlations (e.g., Boué et al., 2013, 2014;
 69 Nishida, 2013). In contrast to previous studies that have primarily discussed the reconstruction of
 70 normal seismic phases from noise correlations, we focus our analysis here on interpretation of a
 71 spurious phase that can be observed from noise correlations between receivers separated at
 72 teleseismic distances. A seismic phase is termed normal if it is present in the Green's function of
 73 the medium, and spurious if it is not observed in real seismograms and does not obey the theory
 74 of seismic wave propagation. First, we correlate seismic noise records from the Full Range
 75 Seismograph Network of Japan (the FNET array) and the northern Fennoscandia
 76 POLENET/LAPNET seismic network (the LAPNET array). Then, we develop a new technique
 77 to analyze the origin of the spurious phase, and propose a mechanism to explain its presence.

78

79 **2 Processing of Noise Data**

80 Continuous seismograms recorded by the broadband stations of the FNET and LAPNET
 81 arrays in 2008 are used to compute the double-array noise correlations (**Figure 1**). The aperture
 82 of LAPNET is ~700 km, and that of FNET is nearly 1,400 km. There are 1,558 FNET–LAPNET
 83 station pairs in all. The distance between the FNET and LAPNET stations ranges from ~56° to
 84 70°, with a center-to-center distance of 63°.

85 Segment-based processing of noise data is demonstrated in **Figure S1**. First, we apply
 86 routine signal-processing operations to the raw seismograms (i.e., mean and linear trend removal,
 87 filtering, 5 Hz down-sampling, instrumental response deconvolution). Then, we divide the
 88 continuous seismograms into 4-hour segments. The frequency spectra of the segments are
 89 whitened between periods of 1 s and 100 s. This spectral whitening removes amplitude
 90 information and retains only the phase spectrum. The whitened waveform is clipped at 3.8 times
 91 the standard deviation. A selection filter is applied to the segments to detect and reject those
 92 containing transient impulses, like earthquakes and electronic glitches.

93 The processing is similar to that adopted by Poli et al. (2012) and Boué et al. (2013). The
 94 main difference is that we use a new kurtosis-based selection filter to detect and reject segments
 95 dominated by impulsive transients. The kurtosis is defined as $\kappa = \mathbf{E}[s^4]/(\mathbf{E}[s^2])^2 - 3$, with $\mathbf{E}[\cdot]$
 96 the expectation operator and s the demeaned waveform. It is highly sensitive to impulsiveness
 97 (Westfall, 2014), close to zero for stationary noise and increases abruptly in the presence of
 98 transient impulses (see **Figure S2** for practical examples). Segments of kurtosis beyond 1.5 are
 99 discarded. In the previous studies, the detection was based on the energy ratio between segment
 100 and daily trace, a coarse version of the classic STA/LTA method for earthquake detection (Allen,
 101 1982). Compared to the energy-based detection, the kurtosis-based detection depends on the
 102 statistics of the amplitudes of the segment itself and is more reliable when the strength of seismic
 103 noise changes rapidly. The kurtosis-based detection has also been used in earthquake detection
 104 (e.g., Baillard et al., 2014; Saragiotis et al., 2002).

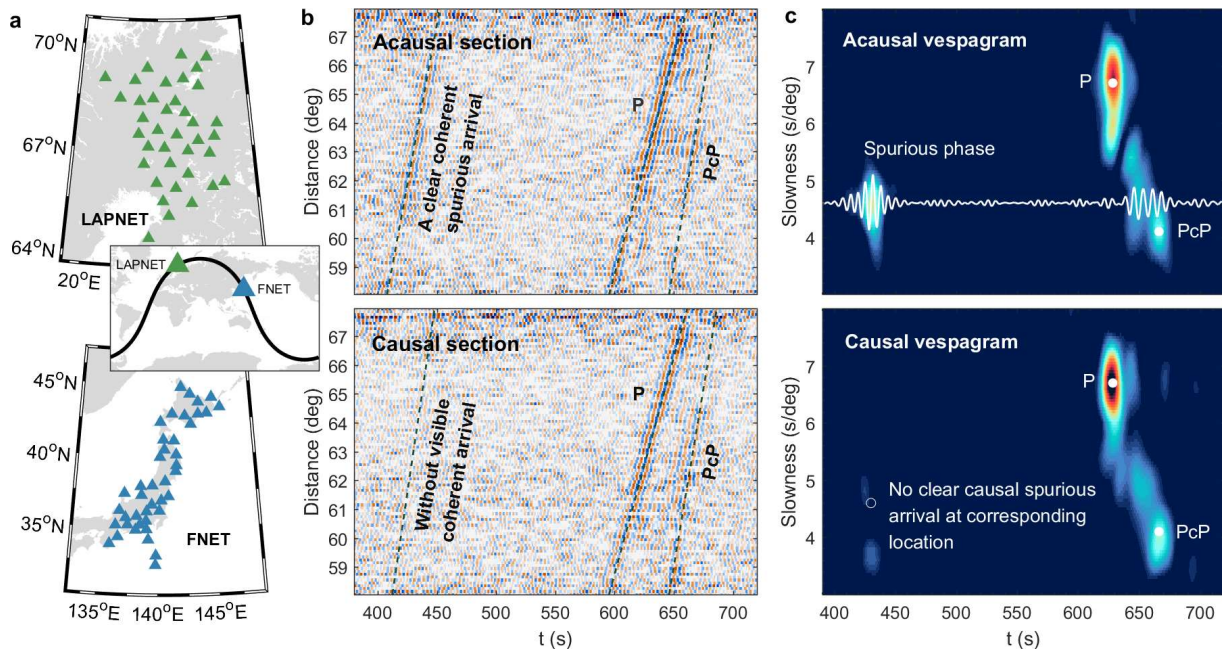
105

106 3 Observation of Noise-Derived Spurious Phase

107 The calculation of correlation function is explained in **Figure S3**. To produce the
 108 correlation function of the year-long data for each FNET–LAPNET station pair, we correlate all
 109 of the available pairs of processed noise segments and stack them. The correlation function has a
 110 causal part and an acausal part. In this paper, the acausal correlations correspond to seismic
 111 waves that travel from FNET to LAPNET (causal: from LAPNET to FNET).

112 The noise correlations of all of the FNET–LAPNET station pairs are binned in an inter-
 113 station distance interval of 0.1° , to produce the waveform sections for the acausal and causal
 114 parts of the noise correlations. The broadband sections of vertical–vertical noise correlations are
 115 shown in **Figure S4** and the filtered sections (periods of 5 s to 10 s) in **Figure 1b**. A coherent
 116 arrival between 410 s and 450 s is clearly visible in the acausal section, about 200 s earlier than
 117 the direct P wave that should be the primary arrival. The arrival has no correspondence in the
 118 true Green’s function of the Earth medium, and thereby is undoubtedly a spurious phase. From
 119 the acausal vespagram in **Figure 1c**, the apparent slowness and emerging time of the spurious
 120 phase at 63° distance can be estimated: ~ 4.6 s/deg and 430 s, respectively. Spectral analysis
 121 indicates that the spurious phase has a peak period of 6.2 s (**Figure S5**), a typical value for the
 122 secondary microseism that is the largest peak in the seismic noise spectra (Peterson, 1993).
 123 Secondary microseisms are dominantly excited by ocean wave–wave interactions (Hasselmann,
 124 1963; Longuet-Higgins, 1950), implying that the noise sources are mainly distributed on the
 125 global ocean surface. In the causal correlations, a corresponding spurious phase is hardly
 126 discriminable.

127



128

129 **Figure 1.** (a) Geographic distributions of the 38 stations of the LAPNET array in Finland, and 41
 130 stations of the FNET array in Japan. Dark line (global map inset), the great circle across the two
 131 networks. (b) Waveform sections and (c) vespagrams of the acausal and causal parts of the
 132 vertical–vertical noise correlations filtered in the secondary microseism period band from 5 s to

133 10 s. Dashed lines (b), predicted time–distance curves. Solid white dots (c), theoretical P and PcP
 134 arrivals, as predicted by the *Taup* program (Crotwell et al., 1999) and the *IASP91* Earth model
 135 (Kennett & Engdahl, 1991). It can be estimated from the acausal vespagram that at 63° distance
 136 between the FNET and LAPNET array centers, the spurious phase has an arrival time of 430 s
 137 and an apparent slowness of 4.6 s/deg. The waveform beamed by 4.6 s/deg slowness is plotted
 138 overlying the acausal vespagram.

139

140 4 Origin of Spurious Phase from P–PKPab Correlations

141 In the previous section, a prominent spurious phase was observed in the FNET–LAPNET
 142 noise correlations, and its apparent slowness and emerging time were estimated. The double-
 143 array configuration provides the possibility to estimate both the azimuths and magnitudes of the
 144 slownesses of the correlated wavefields responsible for the spurious phase. Given a wave with
 145 slowness \mathbf{p}^A at FNET and a wave with slowness \mathbf{p}^B at LAPNET, the time delay between the i th
 146 FNET station and the j th LAPNET station can be determined from Equation (1):

$$147 \quad \Delta t_{ij} = \mathbf{x}_i^A \cdot \mathbf{p}^A + \mathbf{x}_j^B \cdot \mathbf{p}^B \quad (1),$$

148 where \mathbf{x} are the local coordinates of the station with respect to the array center, and superscripts
 149 A and B distinguish between FNET and LAPNET, respectively. For a given pair of $(\mathbf{p}^A, \mathbf{p}^B)$, the
 150 noise correlations of all station pairs are beamed by Equation (2):

$$151 \quad B(t, \mathbf{p}^A, \mathbf{p}^B) = \langle C_{ij}(t - \Delta t_{ij}) \rangle \quad (2),$$

152 where C_{ij} is the correlation function between the i th FNET station and the j th LAPNET station,
 153 and $\langle \cdot \rangle$ indicates the ensemble average. This delay-and-sum process for the double-array data is
 154 known as the double-beam method, which has been applied to earthquake data (e.g., Krüger et
 155 al., 1993; Rost & Thomas, 2002) and noise correlations (e.g., Boué et al., 2013; Roux et al.,
 156 2008). Repeating the double-beamforming for a range of \mathbf{p}^A and \mathbf{p}^B , the power map of the
 157 double-beamed waveforms indicates the optimal slowness estimates for the correlated waves.
 158 Here we call this method the double-array slowness analysis.

159 The results for the spurious phase are shown in **Figure 2a**. The azimuths of the correlated
 160 waves responsible for the spurious phase are confined to the great-circle direction across FNET
 161 and LAPNET, implying that the microseism noise source should be located on the great circle.
 162 The slowness at FNET (4.7 s/deg) is distinct from that at LAPNET (4.2 s/deg). We also apply the
 163 double-array slowness analysis to the acausal P waves (**Figure S6a**). The slownesses of the
 164 interfering waves coincide with each other and are close to the predicted value (6.7 s/deg in
 165 *IASP91* model), as expected for the P–PP correlation in a radially layered Earth structure (**Figure**
 166 **S6b**). The P-wave results justify the reliability of these slowness estimates, and show that lateral
 167 heterogeneity does not cause the slowness discrepancy observed from **Figure 2a**.

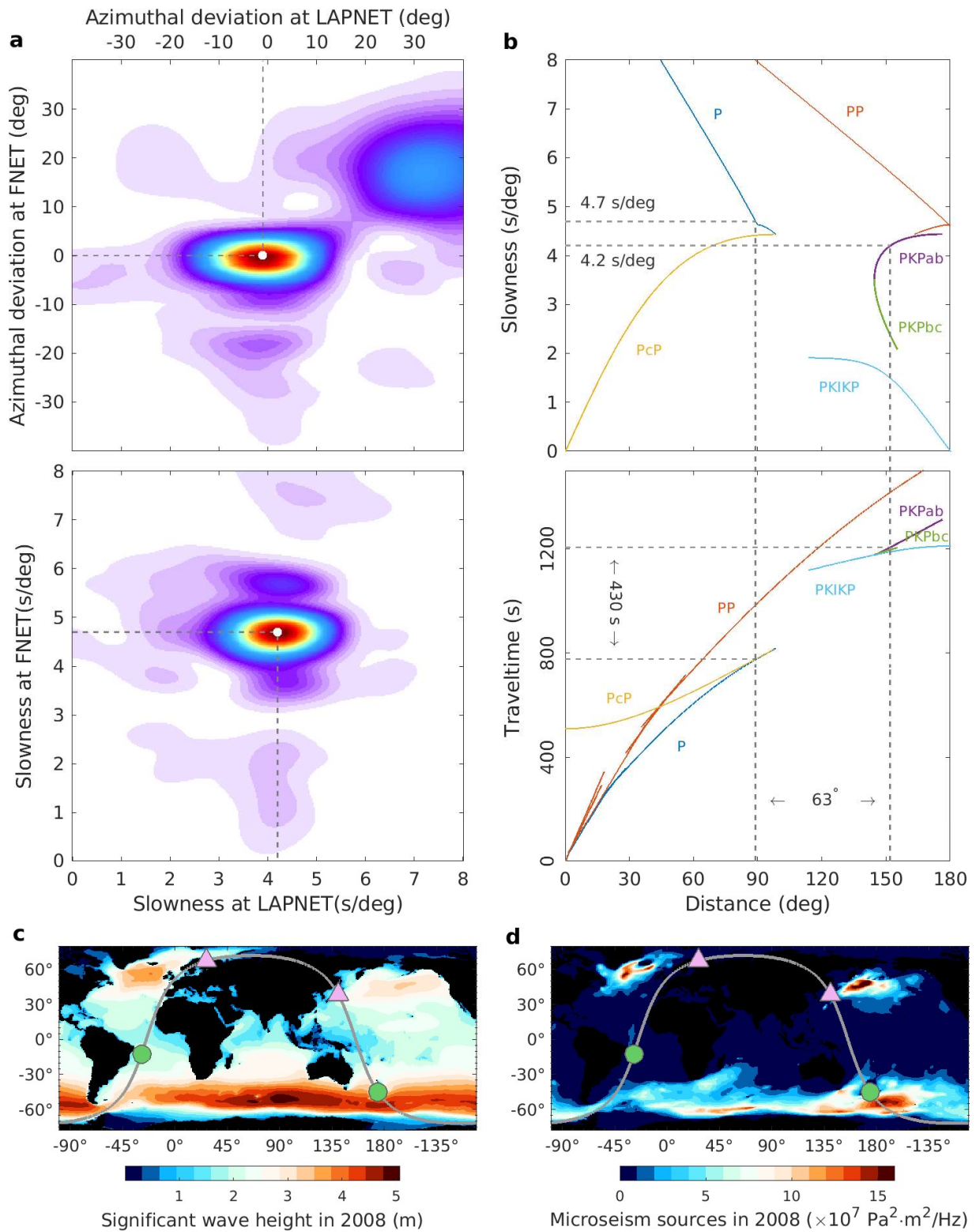
168 The 4.7 s/deg slowness at FNET is valid for deep mantle phases, and the 4.2 s/deg
 169 slowness at LAPNET is characteristic of core phases. We propose a slowness-track method to
 170 seek the ray paths of the interfering waves that produce the spurious phase (**Figure 2b**). All the
 171 body phases that are discernible in the vertical-component earthquake seismograms are
 172 considered as candidates (see labels in **Figure S7**). For a specific seismic phase, the distance
 173 from source to receiver can be derived from the slowness. The pairs of seismic phases are

174 rejected if the difference between the distances from the source to the receivers differs from 63°
175 or if their time delay deviates from 430 s. For clarity, only several typical P-type phases (P, PcP,
176 PP, and PKP branches) are shown in **Figure 2b**.

177 Finally, we find that the correlation between the P wave at $\sim 89^\circ$ distance and the PKPab
178 wave at $\sim 152^\circ$ distance is the only combination that satisfies all the constraints. Thus, we can
179 locate the source responsible for the acausal and causal spurious phase, at around $[45^\circ\text{S}, 174^\circ\text{E}]$
180 and $[12^\circ\text{S}, 28^\circ\text{W}]$, respectively. Recall that the spurious phase is not observable in the causal
181 correlations. Comparisons with hindcast ocean wave heights and microseism excitation (**Figure**
182 **2c, d**) indicate that the time asymmetry can be explained by the difference in the strength of the
183 noise sources: the acausal source in the ocean south of New Zealand is energetic, whereas the
184 causal source in the low-latitude Atlantic east of Brazil is weak.

185 The slownesses estimated from the double-array slowness analysis are crucial for the
186 exclusive determination of the interfering waves. Several pairs of seismic phases will meet the
187 apparent slowness and emerging time of the spurious phase. As can be seen from **Figure 2b**, at
188 89° distance, the PcP wave arrives almost simultaneously with the P wave, which means that
189 PcP–PKPab also has a time delay of ~ 430 s at 63° inter-receiver distance. **Figure S8** shows
190 another example of PcS–PcPPcP that also satisfies the given time delay and inter-station distance
191 as proposed by Pham et al. (2018) for a spurious phase emerging at similar time delay, but in the
192 context of earthquake coda correlations. However, these waves do not match the slownesses
193 estimated from **Figure 2a**. We interpret this such that compared to the prominent direct P and
194 PKPab waves, the core reflections and their surface multiples are faint phases and have minor
195 contributions to the construction of the spurious phase from the noise correlations.

196



197

198 **Figure 2.** (a) Results of the double-array slowness analysis for the acausal spurious phase. White
 199 dots indicate optimal estimates for the azimuths and magnitudes of the slownesses of the

200 interfering waves at FNET and LAPNET that lead to the generation of the spurious phase. The
 201 azimuthal deviation refers to the clockwise azimuthal deviation of slowness from the sagittal
 202 plane crossing FNET and LAPNET. The azimuthal deviations are almost zero. The slowness
 203 values of the interfering waves are 4.7 s/deg at FNET and 4.2 s/deg at LAPNET. **(b)**
 204 Determination of the interfering waves responsible for the spurious phase. The theoretical curves
 205 of the ray parameters and the travel-times are calculated using the *Taup* program and the *IASP91*
 206 Earth model. The global maps show the spatial distributions of **(c)** the significant wave height,
 207 and **(d)** the 6.2 s period secondary microseism excitation in 2008 (Rasche & Arduin, 2013).
 208 Triangles, locations of FNET and LAPNET; circles, locations of the microseism noise sources
 209 responsible for the spurious phase. The source responsible for the acausal spurious phase is
 210 located in the ocean south of New Zealand.

211

212 **5 Quasi-Stationary Phase**

213 The observed spurious phase originates from the correlation between teleseismic P waves
 214 and PKPab waves that emanate from the oceanic microseism noise source south of New Zealand.
 215 In this section, we explain how such spurious signals arise from the interference between waves
 216 of distinct slownesses. Considering the ambient noise wavefield as a superposition of waves
 217 from uncorrelated sources distributed on Earth's surface (**Figure 3a**), the correlation function
 218 between the noise records at two receivers is equivalent to a stack of the correlation functions for
 219 individual sources (source averaging).

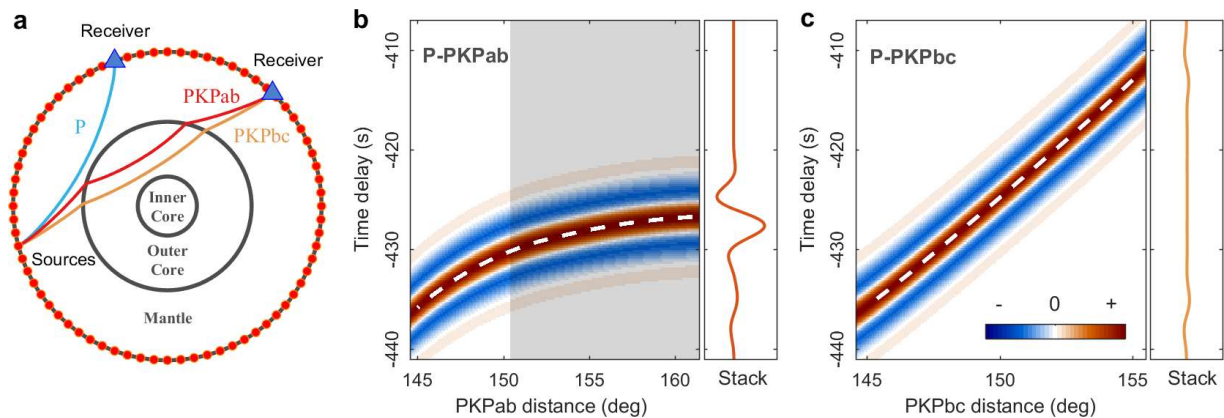
220 We first simulate the source-wise correlation functions by convolving a wavelet of 6.2 s
 221 period with the time delays between the two correlated phases. The final inter-receiver
 222 correlation is obtained by stacking over all sources. In this ray-based simulation, amplitude
 223 information is neglected. The result for the P–PKPab correlations is shown in **Figure 3b**. The
 224 construction of signals from noise correlations has been proposed in relation to the stationary-
 225 phase condition (e.g., Wapenaar et al., 2010). As an illustration, **Figure S6** shows an example of
 226 the reconstruction of the teleseismic P wave that results from the correlation of the P and PP
 227 waves. The reconstruction is linked to the extreme (stationary) point on the curve of the P–PP
 228 time delay. The P and PP waves from the source at the stationary-phase location (**Figure S6**,
 229 source *A*) have a common path and a common slowness. However, as for the spurious phase
 230 observed between FNET and LAPNET, the correlated P and PKPab waves have no slowness or
 231 ray path in common, and there is no stationary point on the curve of the P–PKPab time delay
 232 (**Figure 3b**). The stationary-phase condition is not satisfied, and thus the emergence of the
 233 spurious phase cannot be explained by this argument.

234 **Figure 3b** shows that for finite-frequency waves, the interference between the P and
 235 PKPab waves is constructive over the shaded area; this leads to the pulsive signal in the final
 236 inter-receiver correlation function. In contrast to the condition of stationary phase, we propose to
 237 call this mechanism the condition of quasi-stationary phase, and refer to this range of sources as
 238 the quasi-stationary-phase region or effective source region. At short periods (1 s or shorter),
 239 numerical tests for the P–PKPab correlations indicate that source averaging can still lead to
 240 signals, with narrower effective source region shrinking toward larger source–receiver distances.
 241 Repeating the ray-based modeling in **Figure 3b** for various inter-station distances, a full section
 242 can be obtained for the synthetic P–PKPab correlations (see next section for broadband
 243 simulation result), from which the theoretical time–distance curve of the spurious phase can be

244 picked. The picked curve is the same for the discoid model shown in **Figure 3a** (sources along a
 245 circle) and spherical model (sources on global surface). As shown in **Figure 1b**, the theoretical
 246 time–distance curve fits well to the observed spurious signals.

247 Experiences from earthquake observations indicate that PKPbc waves are generally the
 248 dominant PKP branch at distances from $\sim 144^\circ$ (the PKP-wave caustic) to $\sim 153^\circ$ (Kulháněk,
 249 2002). Microseism studies have also reported that PKPbc waves can be more prominent (e.g.,
 250 Gerstoft et al., 2008; Landés et al., 2010). However, our analysis reveals that the spurious phase
 251 originates from the interference of P waves with PKPab waves, rather than with PKPbc waves.
 252 From the source-averaging experiment for the P–PKPbc correlations (**Figure 3c**), it can be seen
 253 that the P–PKPbc time delay varies almost linearly against the source–receiver distance, and that
 254 the dynamic range of the time delay is broad. Consequently, the signals in the source-wise
 255 correlations are out of phase, which leads to a destructive stack.

256



257

258 **Figure 3.** (a) Geometry of the model to synthesize the inter–receiver correlation function of
 259 teleseismic P and PKP waves via source averaging. (b) P–PKPab correlations for an inter-
 260 receiver distance of 63° . Dashed line, time delays between P and PKPab waves emitted from
 261 distributed sources. Background image shows the source-wise P–PKPab correlation functions
 262 synthesized by convolving the time delays with a 6.2 s period wavelet. The final P–PKPab
 263 correlation function by source averaging is plotted in the right panel. The shaded area indicates
 264 the range of effective sources that contribute to the signal construction. (c) Source-averaging
 265 experiment for the P–PKPbc correlations.

266

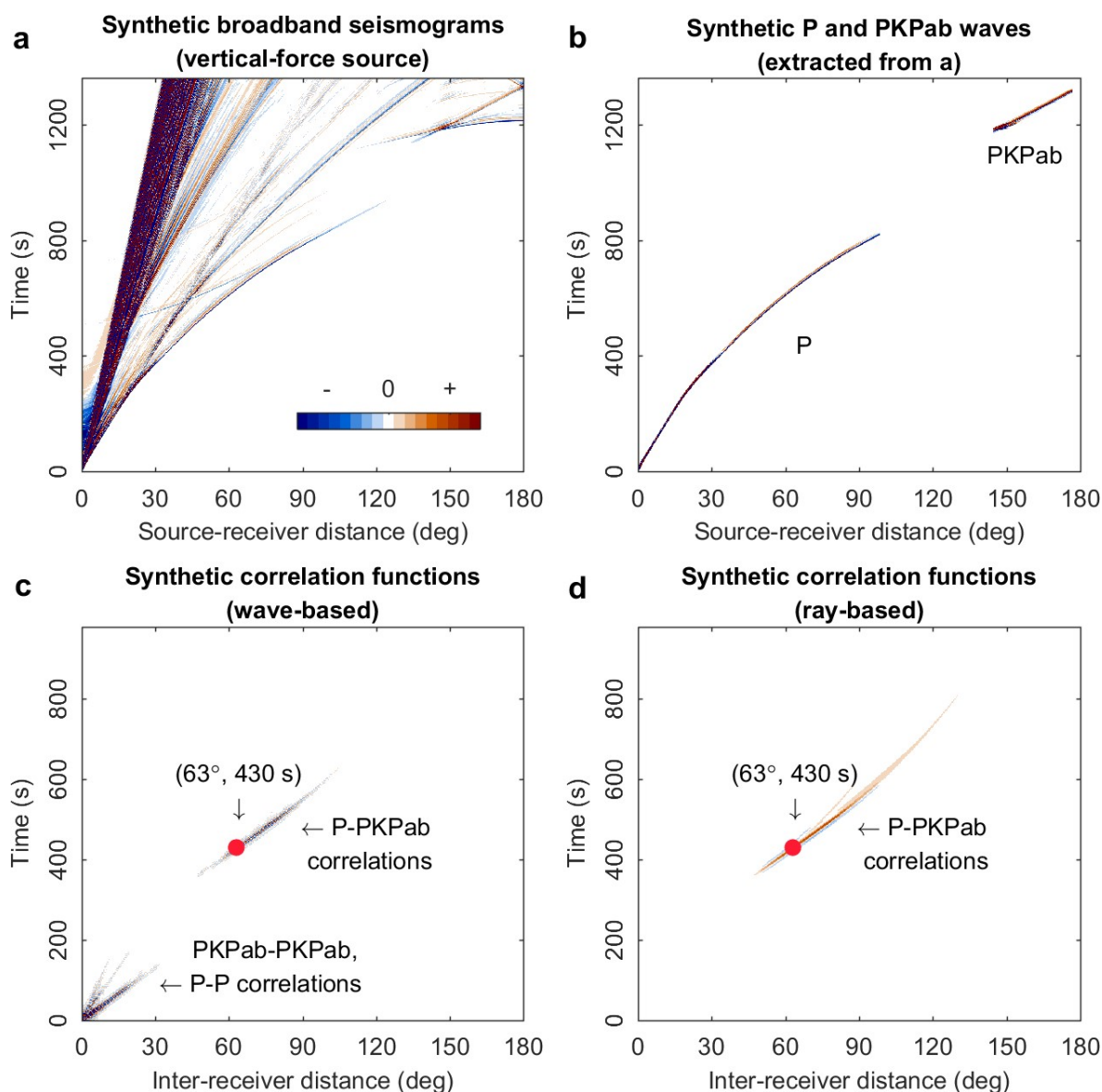
267 6 Effect of Source Distribution

268 **Figure 2d** shows that the spatial distribution of the global microseism sources is heavily
 269 uneven. The spurious phase is observable in the acausal correlations because the corresponding
 270 source is strong, and is not observable in the causal correlations because the responsible source is
 271 too weak. In the ray-based synthetic experiments in **Figure 3**, we have neglected the variations
 272 of amplitude with wave propagations (geometric spread, inelastic attenuation, reflection and
 273 transmission). All of the source-wise correlations are assumed to have the same strength. This
 274 simplification ensures that the spurious phase is not likely to be caused by a strong localized
 275 source. It is worth determining whether the spurious phase can be eliminated with an ideally

276 uniform source distribution. A formal numerical simulation is made with the waveforms of the P
277 and PKPab waves modeled by the spectral-element method. We obtain the vertical components
278 of the global broadband seismogram for the *iasp91_2s* model (**Figure 4a**), from the IRIS
279 Syngine Data Service (Krischer et al., 2017). A mask is applied to the full waveforms to extract
280 the P waves and the PKPab waves (**Figure 4b**). Assuming that the uncorrelated noise sources are
281 distributed evenly on the global surface, we compute the source-wise correlations and stack them
282 for each inter-station distance, using the data in **Figure 4b**. A global section of correlation
283 functions is obtained accordingly (**Figure 4c**). The spurious phase is clearly reproduced, which
284 suggests that it is not caused by unevenly distributed noise sources.

285 The ray-based simulation shown in **Figure 4d** mimics well the emerging times of the
286 spurious signals. However, because of the neglect of amplitude information, this approach over-
287 estimates the range of inter-receiver distances where this spurious phase is observable. The
288 simulation based on the waveform here is undoubtedly more realistic.

289



290

291 **Figure 4.** (a) Synthetic broadband (2-100 s) seismograms obtained from the IRIS Syngine Data
 292 Service. (b) Synthetic seismograms containing P and PKPab only, by muting the other seismic
 293 phases in (a). (c) Synthetic P–PKPab correlations for the various inter-receiver distances using
 294 the waveform data in (b). (d) Synthetic P–PKPab correlations using the ray-based method in
 295 **Figure 3**. Red dot, the observed spurious phase.

296

297 7 Discussions and Perspectives

298 We observe an early spurious arrival in the teleseismic noise correlations between the
 299 Japan and Finland stations. It arises from interference between the ballistic P waves and PKPab
 300 waves that emanate from the oceanic microseism sources south of New Zealand. The interfering
 301 waves have deterministic ray paths that sample the Earth deep structure. It is natural to expect

302 that the spurious phase can also be used to investigate the inner structure of the Earth. The
303 spurious phase is observable in the vertical–vertical noise correlations only, which is logical, as
304 the correlated waves are both P-type and their amplitudes are dominantly projected onto the
305 vertical components.

306 The spurious phase is observable for one side of the correlation functions only. By
307 comparison with oceanic hindcast data, we ascribe this extreme time asymmetry to the large
308 difference in the strength of the microseism sources. The strength of the spurious phase is
309 definitely linked to the microseism excitation in a limited source region. Therefore, another
310 potential application is to monitor the ocean wave activities and microseism excitation.

311 The P–PKPab correlation is not the unique spurious phase in global noise correlations.
312 Multiple spurious arrivals can be observed from the global sections of the noise correlations
313 constructed with both real and synthetic seismograms (Boué et al., 2013, 2014; Ruigrok et al.,
314 2008). The spurious phase observed in this paper is prominent and isolated from other seismic
315 phases, making it a good example to unveil the generation mechanism of such phases. Based on
316 a double-array slowness analysis, we estimated the respective slownesses of the interfering
317 waves, and tracked the responsible noise source back to New Zealand. This method is also
318 applicable to other spurious phases.

319 It is important to emphasize the differences between ambient noise and earthquake coda
320 properties. The late coda waves excited by large earthquakes are composed of high-order modes
321 with small slownesses that correspond to core-related reverberations (Maeda et al., 2006; Boué et
322 al., 2014; Poli et al., 2017). The coda wavefields are quite different from the ambient noise
323 wavefields that are dominated by ballistic waves emanating from the distributed noise sources on
324 the Earth’s surface. Several spurious phases have been observed in late coda correlations and
325 been interpreted with the traditional stationary-phase arguments (e.g., Pham et al., 2018).
326 Dealing with ambient noise correlations at teleseismic distances, we have shown that the
327 spurious phase observed in this study does not correspond to a stationary point. We propose a
328 less restrictive condition of quasi-stationary phase, which explains our finite-frequency
329 observations.

330

331 **Acknowledgments and Data**

332 The seismic data of FNET and LAPNET were provided by the National Research Institute for
333 Earth Science and Disaster Resilience (NIED: <http://www.fnet.bosai.go.jp>) and the Réseau
334 Sismologique & Géodésique Français (RESIF: <http://www.resif.fr>), respectively. The global
335 sections of the earthquake seismograms and synthetic seismograms were obtained from the IRIS
336 Data Services (GlobalStacks: <https://ds.iris.edu/ds/products/globalstacks/>; Syngine:
337 <https://ds.iris.edu/ds/products/syngine/>). The data of hindcast wave heights and synthetic
338 microseism noise sources were provided by IOWAGA products, as described by (Rasclé &
339 Arduin, 2013). The computations were performed using the CIMENT infrastructure
340 (<https://ciment.ujf-grenoble.fr>), which is supported by the Rhône-Alpes region (grant
341 CPER07_13 CIRA: <http://www.ci-ra.org>). This work is supported by a grant from Labex
342 OSUG@2020 (Investissements d’avenir-ANR10LABX56). The authors also acknowledge the
343 support of the Simone and Cino del Duca Foundation, Institut de France.

344

345 **References**

- 346 Allen, R. (1982). Automatic phase pickers: Their present use and future prospects. *Bulletin of the*
347 *Seismological Society of America*, 72(6), S225-242.
- 348 Baillard, C., Crawford, W. C., Ballu, V., Hibert, C., & Mangeney, A. (2014). An automatic
349 kurtosis-based P-and S-phase picker designed for local seismic networks. *Bulletin of the*
350 *Seismological Society of America*, 104(1), 394–409. <https://doi.org/10.1785/0120120347>
- 351 Boué, P., Roux, P., Campillo, M., & de Cacqueray, B. (2013). Double beamforming processing
352 in a seismic prospecting context. *Geophysics*, 78(3), V101–V108.
353 <https://doi.org/10.1190/geo2012-0364.1>
- 354 Boué, P., Poli, P., Campillo, M., Pedersen, H., Briand, X., & Roux, P. (2013). Teleseismic
355 correlations of ambient seismic noise for deep global imaging of the Earth. *Geophysical*
356 *Journal International*, 194(2), 844–848. <https://doi.org/10.1093/gji/ggt160>
- 357 Boué, P., Poli, P., Campillo, M., & Roux, P. (2014). Reverberations, coda waves and ambient
358 noise: correlations at the global scale and retrieval of the deep phases. *Earth and Planetary*
359 *Science Letters*, 391, 137–145. <https://doi.org/10.1016/j.epsl.2014.01.047>
- 360 Brenguier, F., Campillo, M., Hadziioannou, C., Shapiro, N. M., Nadeau, R. M., & Larose, E.
361 (2008). Postseismic relaxation along the San Andreas Fault at Parkfield from continuous
362 seismological observations. *Science*, 321(5895), 1478–1481.
363 <https://doi.org/10.1126/science.1160943>
- 364 Campillo, M., & Paul, A. (2003). Long-range correlations in the diffuse seismic coda. *Science*,
365 299(5606), 547–549. <https://doi.org/10.1126/science.1078551>
- 366 Campillo, M., & Roux, P. (2015). Crust and Lithospheric Structure - Seismic Imaging and
367 Monitoring with Ambient Noise Correlations. In *Treatise on Geophysics* (pp. 391–417).
368 <https://doi.org/10.1016/B978-0-444-53802-4.00024-5>
- 369 Crotwell, H. P., Owens, T. J., & Ritsema, J. (1999). The TauP Toolkit: flexible seismic travel-
370 time and ray-path utilities. *Seismological Research Letters*, 70(2), 154–160.
371 <https://doi.org/10.1785/gssrl.70.2.154>
- 372 Gerstoft, P., Shearer, P. M., Harmon, N., & Zhang, J. (2008). Global P, PP, and PKP wave
373 microseisms observed from distant storms. *Geophysical Research Letters*, 35(23), 4–9.
374 <https://doi.org/10.1029/2008GL036111>
- 375 Hasselmann, K. (1963). A statistical analysis of the generation of microseisms. *Reviews of*
376 *Geophysics*, 1(2), 177–210. <https://doi.org/10.1029/RG001i002p00177>
- 377 Kennett, B., & Engdahl, E. R. (1991). Traveltimes for global earthquake location and phase
378 identification. *Geophysical Journal International*, 105(2), 429–465.
379 <https://doi.org/10.1111/j.1365-246X.1991.tb06724.x>
- 380 Krischer, L., Hutko, A. R., van Driel, M., Stähler, S., Bahavar, M., Trabant, C., & Nissen-Meyer,
381 T. (2017). On-demand custom broadband synthetic seismograms. *Seismological Research*
382 *Letters*, 88(4), 1127–1140. <https://doi.org/10.1785/0220160210>

- 383 Krüger, F., Weber, M., Scherbaum, F., & Schlittenhardt, J. (1993). Double beam analysis of
384 anomalies in the core-mantle boundary region. *Geophysical Research Letters*, 20(14),
385 1475–1478. <https://doi.org/10.1029/93GL01311>
- 386 Kulháněk, O. (2002). The structure and interpretation of seismograms. In *International*
387 *Geophysics* (Vol. 81, pp. 333–348). Elsevier B.V. <https://doi.org/10.1016/S0074->
388 6142(02)80224-8
- 389 Landés, M., Hubans, F., Shapiro, N. M., Paul, A., & Campillo, M. (2010). Origin of deep ocean
390 microseisms by using teleseismic body waves. *Journal of Geophysical Research: Solid*
391 *Earth*, 115(5), 1–14. <https://doi.org/10.1029/2009JB006918>
- 392 Lobkis, O. I., & Weaver, R. L. (2001). On the emergence of the Green's function in the
393 correlations of a diffuse field. *The Journal of the Acoustical Society of America*, 110(6),
394 3011–3017. <https://doi.org/10.1121/1.1417528>
- 395 Longuet-Higgins, M. S. (1950). A theory of the origin of microseisms. *Philosophical*
396 *Transactions of the Royal Society A: Mathematical, Physical and Engineering Sciences*,
397 243(857), 1–35. <https://doi.org/10.1098/rsta.1950.0012>
- 398 Maeda, T., Sato, H., & Ohtake, M. (2006). Constituents of vertical-component coda waves at
399 long periods. *Pure and Applied Geophysics*, 163(2–3), 549–566.
400 <https://doi.org/10.1007/s00024-005-0031-9>
- 401 Nishida, K. (2013). Global propagation of body waves revealed by cross-correlation analysis of
402 seismic hum. *Geophysical Research Letters*, 40(9), 1691–1696.
403 <https://doi.org/10.1002/grl.50269>
- 404 Peterson, J. (1993). Observations and modeling of seismic background noise. *U.S. Geol. Surv.*
405 *Open File Report 93-322*, (No. 93-322).
- 406 Phạm, T.-S., Tkalčić, H., Sambridge, M., & Kennett, B. (2018). Earth's correlation wavefield:
407 late coda correlation. *Geophysical Research Letters*, 45(7), 3035–3042.
408 <https://doi.org/10.1002/2018GL077244>
- 409 Poli, P., Campillo, M., & Pedersen, H. (2012). Body-wave imaging of Earth's mantle
410 discontinuities from ambient seismic noise. *Science*, 338(6110), 1063–1065.
411 <https://doi.org/10.1126/science.1228194>
- 412 Poli, P., Campillo, M., & de Hoop, M. (2017). Analysis of intermediate period correlations of
413 coda from deep earthquakes. *Earth and Planetary Science Letters*, 477, 147–155.
414 <https://doi.org/10.1016/j.epsl.2017.08.026>
- 415 Rasche, N., & Arduin, F. (2013). A global wave parameter database for geophysical
416 applications. Part 2: model validation with improved source term parameterization. *Ocean*
417 *Modelling*, 70, 174–188. <https://doi.org/10.1016/j.ocemod.2012.12.001>
- 418 Rost, S., & Thomas, C. (2002). Array seismology: methods and applications. *Reviews of*
419 *Geophysics*, 40(3), 1008. <https://doi.org/10.1029/2000RG000100>
- 420 Roux, P., Cornuelle, B. D., Kuperman, W. a, & Hodgkiss, W. S. (2008). The structure of raylike
421 arrivals in a shallow-water waveguide. *The Journal of the Acoustical Society of America*,
422 124(6), 3430–3439. <https://doi.org/10.1121/1.2996330>

- 423 Ruigrok, E., Draganov, D., & Wapenaar, K. (2008). Global-scale seismic interferometry: theory
424 and numerical examples. *Geophysical Prospecting*, *56*(3), 395–417.
425 <https://doi.org/10.1111/j.1365-2478.2008.00697.x>
- 426 Sabra, K. G., Gerstoft, P., Roux, P., Kuperman, W. A., & Fehler, M. C. (2005). Surface wave
427 tomography from microseisms in Southern California. *Geophysical Research Letters*,
428 *32*(14), 1–4. <https://doi.org/10.1029/2005GL023155>
- 429 Saragiotis, C. D., Hadjileontiadis, L. J., & Panas, S. M. (2002). PAI-S/K: A robust automatic
430 seismic P phase arrival identification scheme. *IEEE Transactions on Geoscience and*
431 *Remote Sensing*, *40*(6), 1395–1404. <https://doi.org/10.1109/TGRS.2002.800438>
- 432 Shapiro, N. M., & Campillo, M. (2004). Emergence of broadband Rayleigh waves from
433 correlations of the ambient seismic noise. *Geophysical Research Letters*, *31*(7), 8–11.
434 <https://doi.org/10.1029/2004GL019491>
- 435 Shapiro, N. M. N., Campillo, M., & Stehly, L. (2005). High-resolution surface-wave tomography
436 from ambient seismic noise. *Science*, *307*(5715), 1615–1618.
437 <https://doi.org/10.1126/science.1108339>
- 438 Wapenaar, K. (2004). Retrieving the elastodynamic Green's function of an arbitrary
439 inhomogeneous medium by cross correlation. *Physical Review Letters*, *93*(25), 254301.
440 <https://doi.org/10.1103/PhysRevLett.93.254301>
- 441 Wapenaar, K., Draganov, D., Snieder, R., Campman, X., & Verdel, A. (2010). Tutorial on
442 seismic interferometry: Part 1 — Basic principles and applications. *Geophysics*, *75*(5),
443 75A195-75A209. <https://doi.org/10.1190/1.3457445>
- 444 Wegler, U., Nakahara, H., Sens-Schönfelder, C., Korn, M., & Shiomi, K. (2009). Sudden drop of
445 seismic velocity after the 2004 Mw6.6 mid-Niigata earthquake, Japan, observed with
446 Passive Image Interferometry B06305. *Journal of Geophysical Research: Solid Earth*,
447 *114*(6), B06305. <https://doi.org/10.1029/2008JB005869>
- 448 Westfall, P. H. (2014). Kurtosis as peakedness, 1905–2014. R.I.P. *The American Statistician*,
449 *68*(3), 191–195. <https://doi.org/10.1080/00031305.2014.917055>
450



Geophysical Research Letters

Supporting Information for

Spurious Arrival in Teleseismic Noise Correlations Explained by a Quasi-Stationary Phase Condition

Lei Li, Pierre Boué, and Michel Campillo

Université Grenoble Alpes, CNRS, IRD, IFSTTAR, ISTerre, 38000 Grenoble, France.

Contents of this file

Figures S1 to S8.

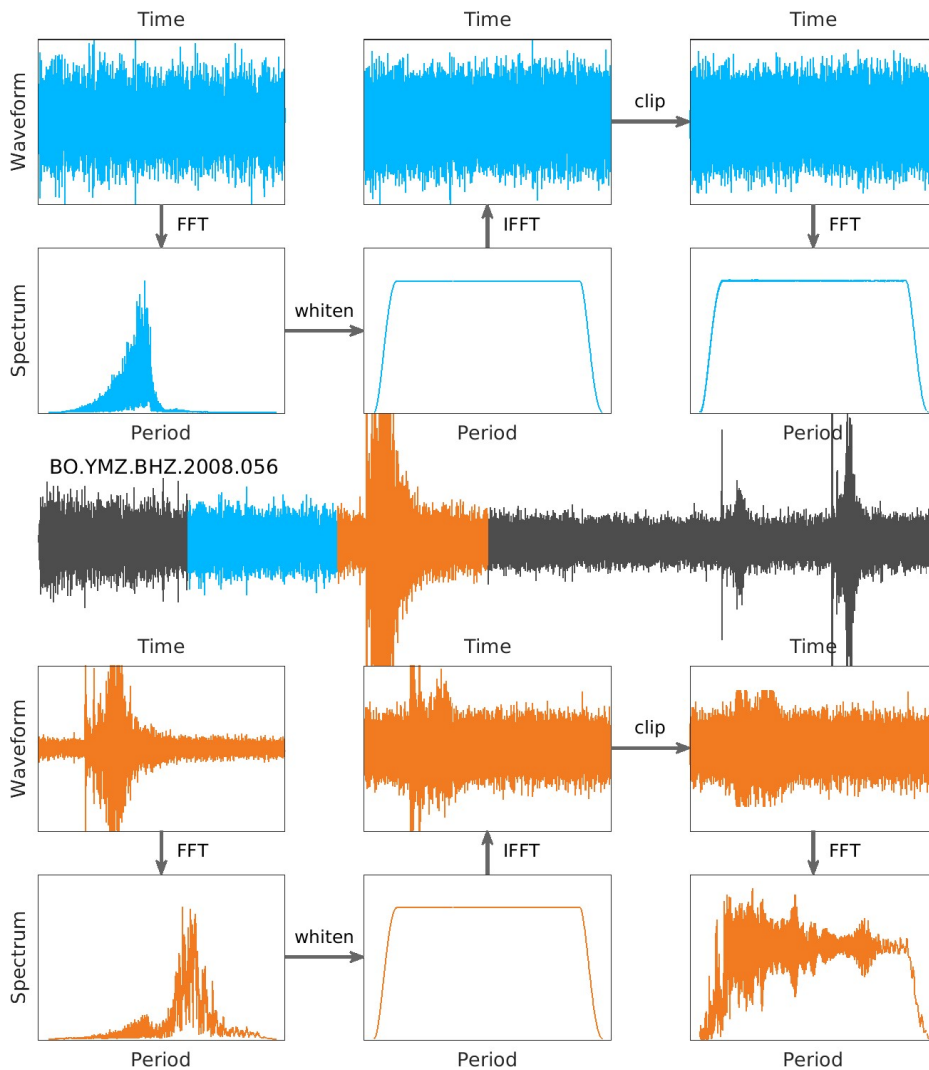


Figure S1. Segment-based noise data processing. A segment with stationary noise and a segment containing a M7.2 teleseism from a daily trace recorded by FNET station BO.YMZ are used for demonstration. The continuous seismogram is demeaned, detrended, bandpass filtered, 5 Hz resampled and instrumental-response removed. Then it is divided into 4-hr segments and their frequency spectra are whitened between 1 and 100 s. One may further clip the spectral-whitened waveform at several times of the standard deviation. The clipping is useful in suppressing large amplitudes in segments with large transients, but has little effect on stationary noise. Thus, the clipping is optional, depending on whether to retain segments with few local spikes. A kurtosis-based selection filter is used to detect and reject segments containing transient impulses like earthquakes and electronic glitches.

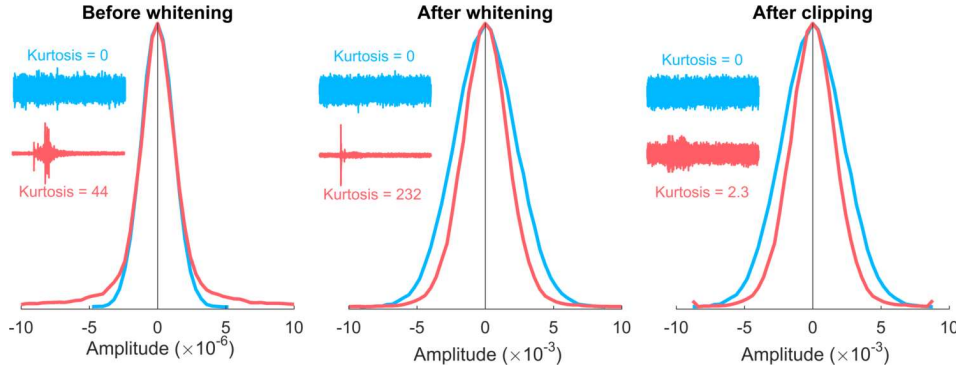


Figure S2. Kurtosis-based selection filter to determine if a segment contains large-amplitude transients. The two segments used here are the same as in Figure S1. The amplitude histograms of the original, spectral-whitened and clipped waveforms are shown in the left, middle and right panels, respectively. For display, waveforms are plotted in different scales. Amplitude histograms are normalized by their own maximums. Histogram tails outside the horizontal axis limits are cropped. The values of kurtosis are labeled. The kurtosis-based selection filter is implemented by rejecting segments with kurtosis beyond a threshold. The selection filter can be applied to any one or more of the three stages shown here. In this paper, we choose a threshold of 1.5 for the clipped segments.

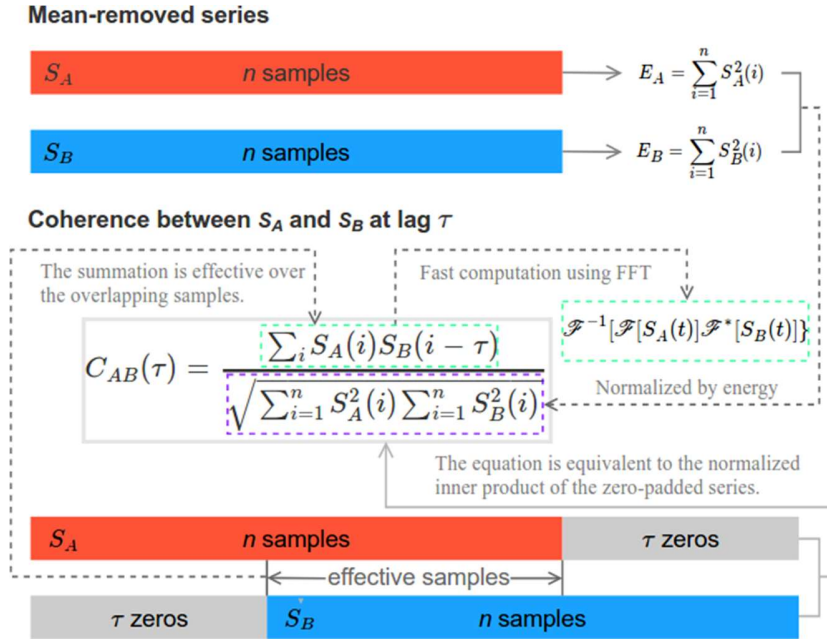


Figure S3. Schematic diagram explaining the computation of correlation function between two mean-removed series. The computation can either be done in the time domain or in the frequency domain. In seismic interferometry, it is common to utilize the Fast Fourier Transform (FFT) for a faster computation of noise correlations. The correlation function contains coherence values for both positive and negative lags between two correlated time series. The part of correlation function at positive (negative) lags is termed causal (acausal).

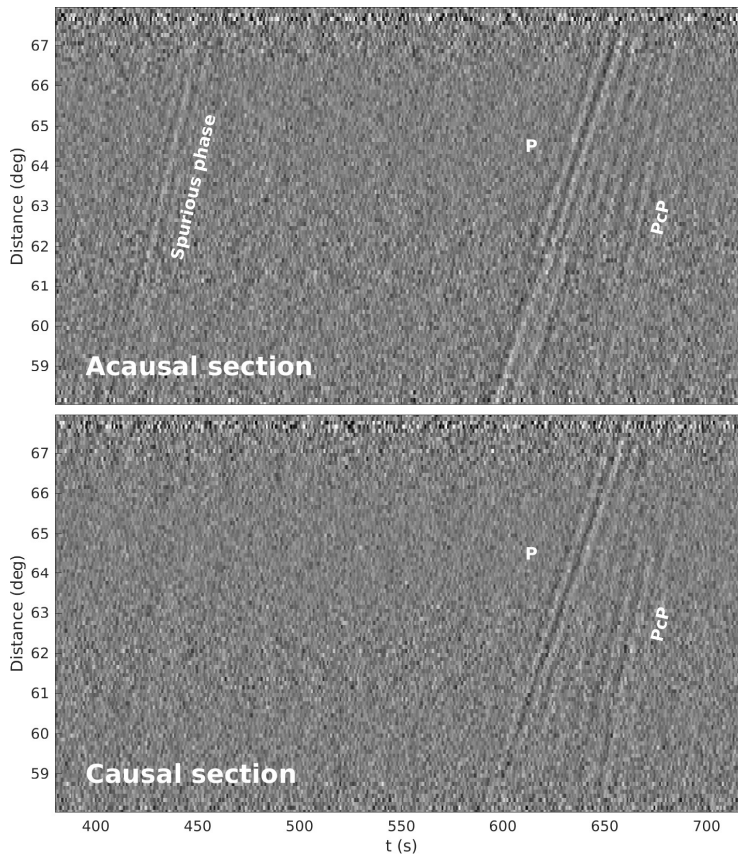


Figure S4. Broadband sections of the acausal and causal parts of the vertical-vertical noise correlations stacked in 0.1° distance bins. The acausal section for negative time lags is flipped to share a common time axis with the causal section. The acausal (causal) correlations correspond to seismic waves travelling from FNET to LAPNET (from LAPNET to FNET).

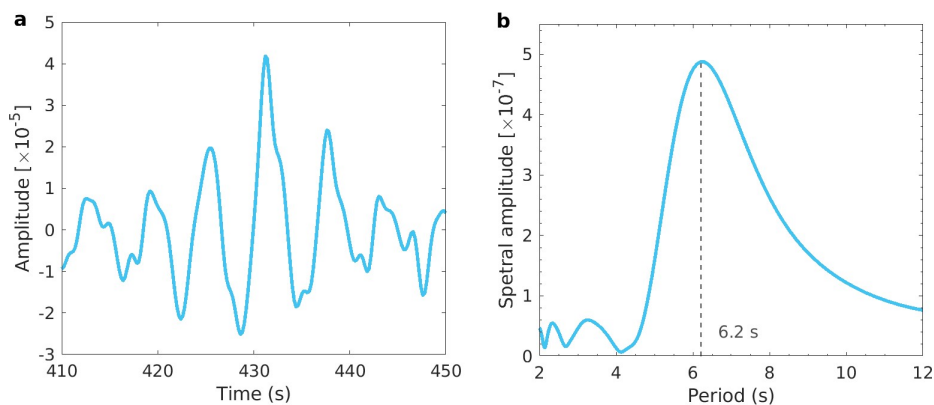


Figure S5. (a) Double-beamed waveform and (b) amplitude spectrum of the spurious phase in the broadband (1-100 s).

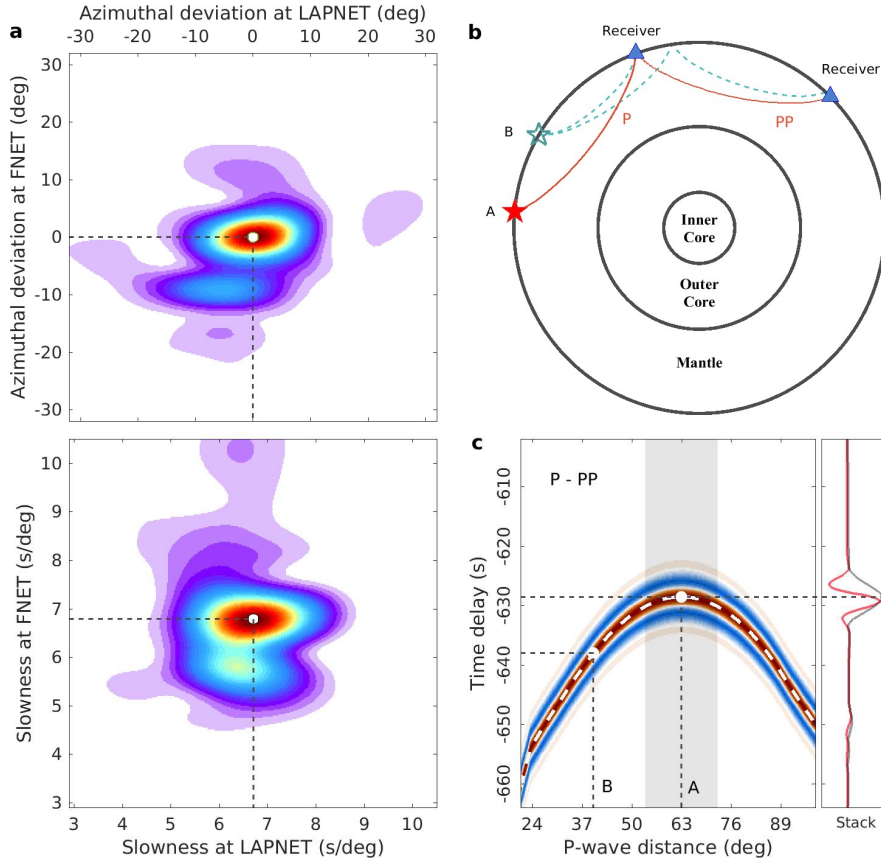


Figure S6. (a) Results of double-array slowness analysis for the acausal P wave. The optimal estimates are marked by white dots. (b) Ray paths of the correlated P and PP waves from distributed sources. Triangles are two receivers 63° apart. Stars represent noise sources. Source *A* is placed at the stationary location. The P wave to the first receiver and the PP wave to the second receiver have a common slowness and a common P path. The correlation operator cancels the common path and extracts the phase delay between two receivers. Label *B* denotes any noise source on the global surface outside the stationary-phase region. Correlations between higher-order multiples like PP-PPP can also give rise to P wave but are neglected for simplicity. (c) Reconstruction of the inter-receiver P wave from the correlations between P and PP waves by source averaging, explained by the traditional stationary-phase theory. Dashed white line indicates the theoretical P-PP time delays for distributed noise sources, calculated using *Taup* and *IASP91*. The stationary location corresponds to the extreme point on the time-delay curve. Columns of the background image are synthetic P-PP correlations for distributed sources. Red and blue colors signify positive and negative amplitudes, respectively. The source-wise correlation functions are synthesized by convolving the time delays with a 6.2 s period Gaussian-modulated sinusoidal pulse. Amplitude variations with distance are neglected. Shaded area delineates the stationary-phase region that contribute to the reconstruction of the inter-receiver P wave. Amplitudes in P-PP correlations for sources outside the stationary-phase region cancel out by the averaging. The inter-receiver P-wave signal (red) and its envelope (black) are plotted in the right panel. The time at the maximum of the envelope matches exactly with the theoretical travel time of the P wave.

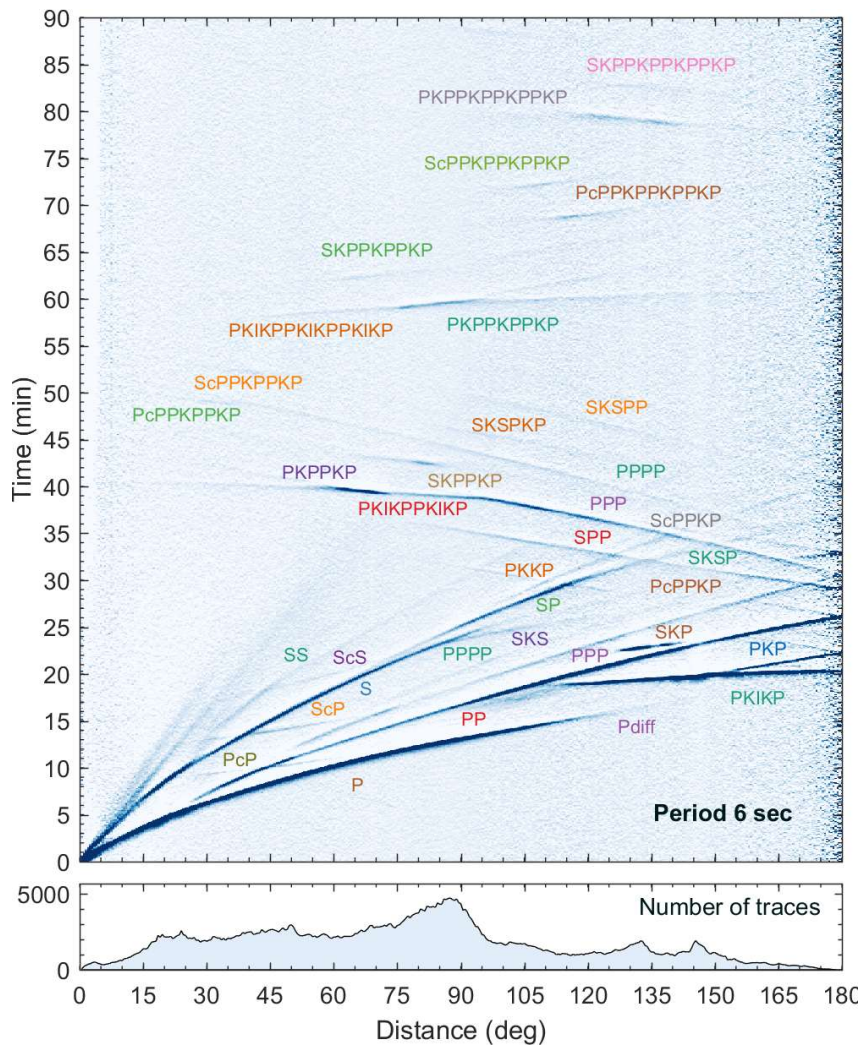


Figure S7. Global stacks of vertical components of seismograms selected from records of more than 2,500 shallow earthquakes (event depth shallower than 50 km and magnitude no less than 5.4) occurring between 1995 and 2013. The seismograms are filtered around 6 s period and converted into traces of STA/LTA ratios. The STA/LTA traces are binned by epicentral distances in an interval of 0.5° and normalized for plotting. More details concerning the data processing and data retrieval can be found on the IRIS Data Services Products website. Discernible seismic body phases are labeled on the image.

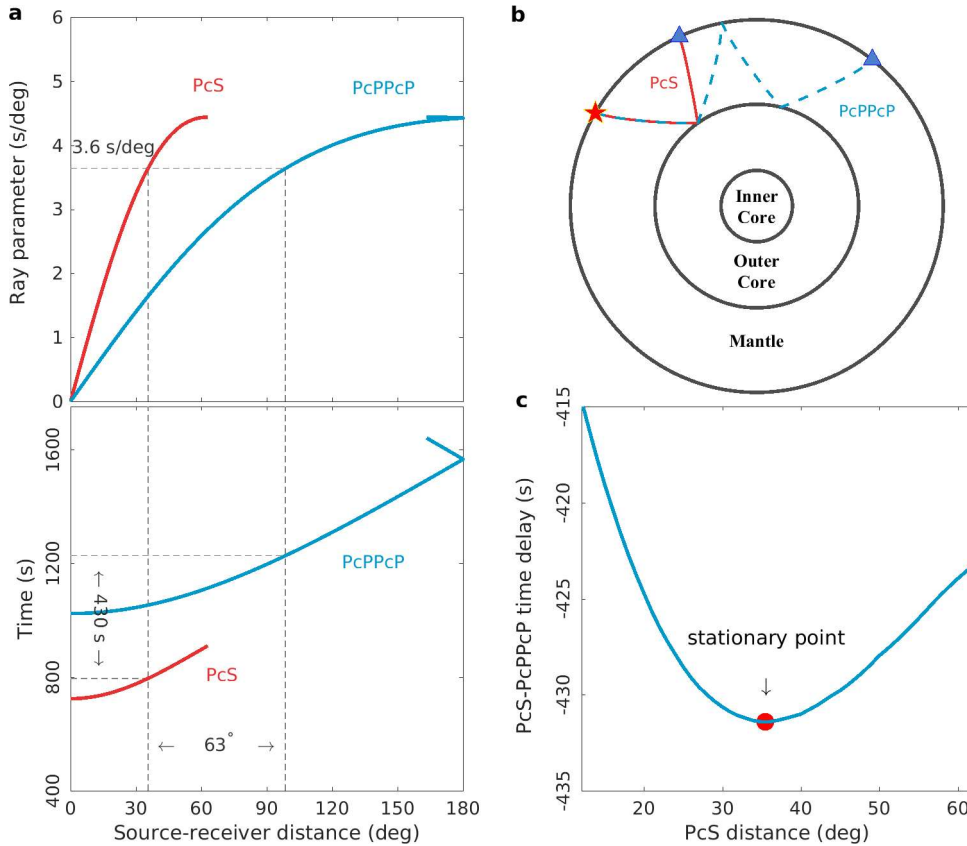


Figure S8. (a) Theoretical curves of ray parameters and travel times of PcS and PcPPcP. (b) Ray paths of PcS and PcPPcP from source at stationary location. (c) PcS-PcPPcP time delays for distributed sources. The PcS-PcPPcP correlation can produce a signal at 430 s time delay and 63° inter-station distance, but the slownesses are quite different from out slowness estimates in Figure 2a. In the global section of coda correlations [see Figure 2 of Phạm et al. (2018)], there is a spurious arrival at ~430 s time delay and 63° distance. Phạm et al. (2018) ascribed the arrival to cS-cPPcP (or s-pPcP in IASPEI convention) correlations for sources distributed on the core-mantle boundary. The PcS-PcPPcP correlation here is an equivalence to their cS-cPPcP correlation, but for sources on the surface. PcS and PcPPcP waves could be prominent in the period band of 30-50 s in the coda waves of large earthquakes, but are faint phases in the ambient wavefield. Therefore, it is logical that we do not observe the PcS-PcPPcP correlations from the ambient noise correlations.